Applied Catalysis B: Environment and Energy 371 (2025) 125262

Contents lists available at ScienceDirect

Applied Catalysis B: Environment and Energy

journal homepage: www.elsevier.com/locate/apcatb

Nb_2C MXene quantum dots modulate built-in electric field within heterostructures for efficient solar-to-H_2O_2 conversion from seawater

Yamei Huang [a], Xinglin Wang [a], Huihui Zhang [a], Linlin Gao [a], Jiayi Meng [a], Yifan Liao [a], Quanmei Zhou [a], Yuchen Wei [a], Baoning Zong [c,*], Hexing Li [b,*], Wei-Lin Dai [a,*]

[a] *Department of Chemistry and Shanghai Key Laboratory of Molecular Catalysis and Innovative Materials, Fudan University, Shanghai 200438, China*
[b] *Key Laboratory of Resource Chemistry of Ministry of Education Shanghai Key Laboratory of Rare Earth Functional Materials College of Chemistry and Materials Science, Shanghai Normal University, Shanghai 200234, China*
[c] *Research Institute of Petroleum Processing, Sinopec, Beijing 100083, China*

ARTICLE INFO

Keywords:
Nb_2C MXene quantum dots
Built-in electric field
H_2O_2 photosynthesis
Synergistic effect

ABSTRACT

Artificial photosynthesis of H_2O_2 from inexhaustible seawater is a desirable energy production strategy, but substantial challenge. Herein, we present the Nb_2C quantum dots anchored on pyrene-based covalent organic framework (Nb_2C QDs@PY-DHBD-COF, NQPD-x) heterostructures for efficient non-sacrificial H_2O_2 photosynthesis directly from air and seawater. The optimal NQPD-3 catalyst achieves an impressive H_2O_2 production rate of 3560 μmol g^{-1} h^{-1}, and apparent quantum yield of 12.8 % at 400 nm together with solar-to-chemical conversion efficiency of 0.27 %, surpassing most previously reported photocatalysts. Expanding further, the utilization of NQPD-3 polypropylene nonwoven fabric membranes for fabricating photocatalytic device show promising potential in practical large-scale application. Combining advanced characterizations with theoretical calculations verify that the excellent photocatalytic performance is ascribed to the robust built-in electric field modulated by Nb_2C QDs, and the synergistic effect of heterostructures, inducing photo-generated carriers transfer and optimizing O_2 adsorption. This work provides a perspective for highly efficient and practical photocatalysts for H_2O_2 production from earth-abundant seawater in a sustainable way.

1. Introduction

Hydrogen peroxide (H_2O_2) is a critical chemical, with global annual production reaching 48 million metric tons, which serves as a versatile and eco-friendly oxidant with broad applications in chemical synthesis, wastewater treatment and clean fuels [1–3]. The conventional route for industrial H_2O_2 production is through multistep anthraquinone oxidation process, which suffers from intensive energy consumption, complex processes, and toxic by-products [4–8]. Alternatively, the artificial photosynthesis of H_2O_2 via employing H_2O and O_2 without sacrificial agents is a prospective strategy to replace the traditional routes [9–12]. Given the abundance of seawater, utilizing seawater for H_2O_2 photosynthesis can not only mitigates the shortage of fresh water resource but also meets sustainable development [13,14]. Nonetheless, the direct H_2O_2 photosynthesis from inexhaustible seawater remains limited and still in its infancy, while the photocatalytic efficiency is still unsatisfactory for the large-scale industrial production [15]. It is imperative to exploit low-cost and efficient photocatalysts for tackling the challenges of practical H_2O_2 production from natural seawater.

Covalent organic frameworks (COFs) featured by customizable optoelectronic properties and active site architectures, have emerged as promising candidate for photocatalytic H_2O_2 production [16–21]. Among these, the pyrene-based COFs exhibit considerable potential in photocatalytic reactions, but typically suffer from low charge-generation and -transfer efficiencies as well as rapid charge recombination, which restricts the application for photocatalytic H_2O_2 production [22,23]. Therefore, the interfacial modulating strategies such as introducing suitable sites and constructing heterojunction are beneficial to promote the photoexcitation and charge separation/transfer for COFs-based photocatalysts, facilitating H_2O_2 photoproduction [24,25]. In recent years, the emerging two-dimensional transition metal carbides, nitrides and carbonitrides (MXenes) have attracted extensive concern in photocatalysis field attributed to the tunable elemental composition and excellent photoelectric properties [26–28]. The zero-dimensional quantum dots (MQDs) derived from MXenes not only inherit the superiority of MXenes but also show better

---

* Corresponding authors.
E-mail addresses: Zongbn.ripp@sinopec.com (B. Zong), Hexing-Li@shnu.edu.cn (H. Li), wldai@fudan.edu.cn (W.-L. Dai).

https://doi.org/10.1016/j.apcatb.2025.125262
Received 9 January 2025; Received in revised form 27 February 2025; Accepted 12 March 2025
Available online 15 March 2025

dispersibility, light absorption ability, excellent electron transport property, high stability and easier functionalization ascribed to the quantum confinement effect [29,30]. Therefore, the rational design of abundant MQDs active sites incorporated into COFs for direct H_2O_2 photosynthesis from inexhaustible seawater is unprecedented and challenging.

Herein, a facile and economical strategy is provided for the build of Nb_2C QDs active sites anchored on pyrene-based COF (Nb_2C QDs@PY-

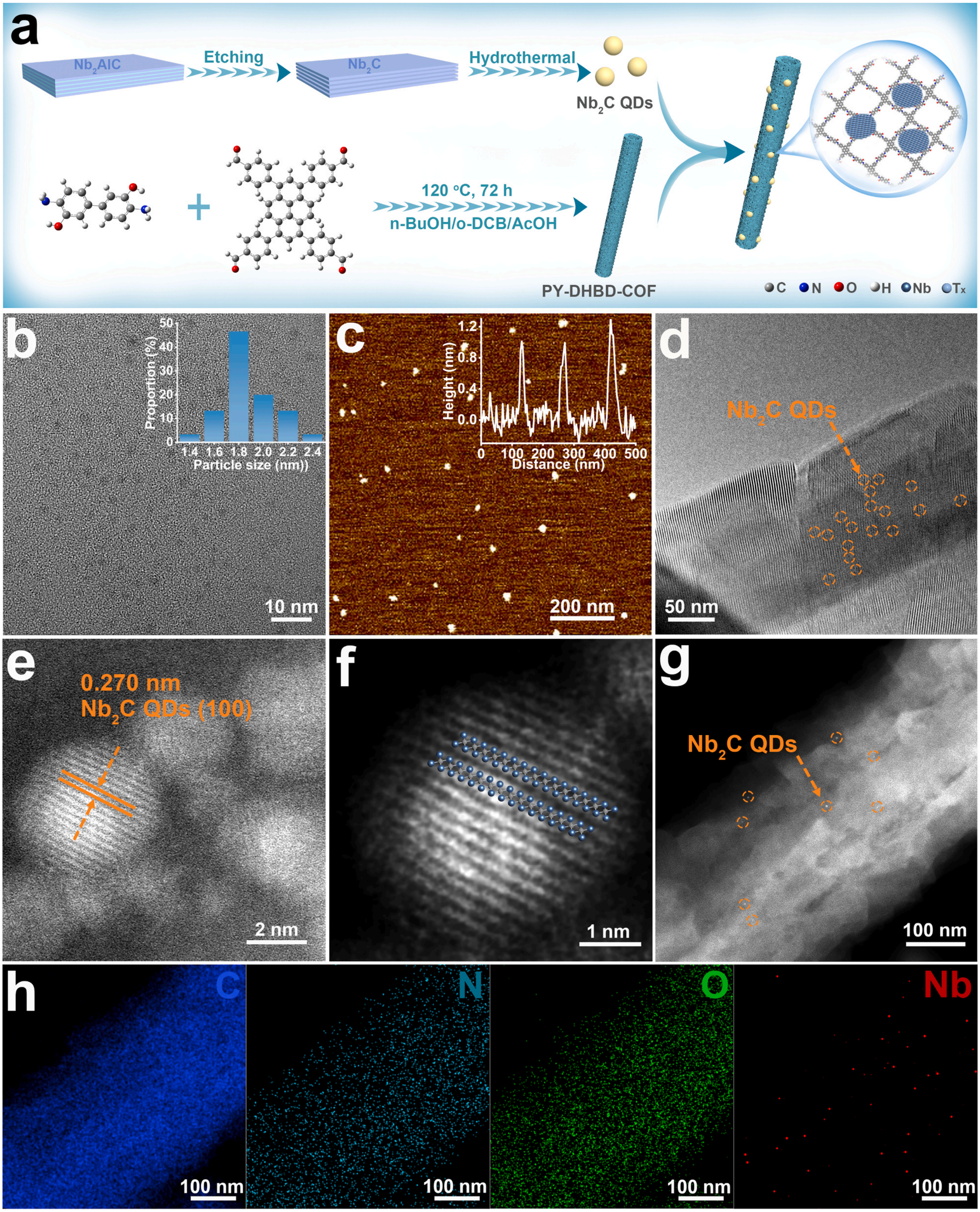

Fig. 1. (a) Schematic illustration of Nb_2C QDs@PY-DHBD-COF synthesis. (b) TEM image of Nb_2C QDs (inset: size distribution). (c) AFM image of Nb_2C QDs. (d) TEM image of NQPD-3. (e) AC-STEM image of NQPD-3. (f) AC-HAADF-STEM image of NQPD-3. (g) HAADF-STEM image of NQPD-3. (h) EDX elemental mappings of NQPD-3.

DHBD-COF, NQPD-x) heterostructures to boost the non-sacrificial H_2O_2 photosynthesis from air and natural seawater. The optimal NQPD-3 catalyst exhibits excellent H_2O_2 generation rate of 3560 μmol g^{-1} h^{-1} under visible-light irradiation, achieving an apparent quantum yield of 12.8 % at 400 nm together with solar-to-chemical conversion efficiency of 0.27 %, which far surpasses the most reported photocatalysts. Combining advanced characterizations with theoretical calculations, the outstanding photocatalytic activity is ascribed to the robust built-in electric field triggered by Nb_2C QDs, and the synergistic effect of heterostructures, inducing photo-generated carriers transfer and optimizing O_2 adsorption. This work offers a protocol for designing efficient photocatalysts and achieving sustainable H_2O_2 production from air and natural seawater.

2. Experimental section

2.1. Synthesis of Nb_2C QDs

The Nb_2AlC powder (1 g) was added slowly to HF solution (30 mL, 40 wt%) and stirred constantly. The mixture was reacted at 35 °C for 48 h, and washed with deionized water and centrifuged (3500 rpm, 5 min) several times until pH> 6, and obtained Nb_2C MXene powder via freeze drying. Then, the Nb_2C MXene powder (0.2 g) was dispersed into deionized water (30 mL) and sonicated for 1 h in the presence of Ar-protection gas. The above mixture was transferred into a Teflon-lined autoclave, and added ammonium hydroxide (2 mL). The autoclave was sealed off and kept at 120 °C for 6 h. Then, the mixture was filtered with 0.22 μm polytetrafluoroethylene membrane, and the filtrate was dialyzed in 500 Da dialysis bag for 24 h to obtain Nb_2C QDs.

2.2. Synthesis of PY-DHBD-COF

The 1,4-dihydroxybenzidine (0.04 mmol, 8.6 mg) and 1,3,6,8-tetra(4-formylphenyl)pyrene (0.02 mmol, 12.3 mg) were combined in a mixture of *n*-butyl alcohol (*n*-BuOH), *o*-dichlorobenzene (*o*-DCB) and 6 M acetic acid (0.5, 0.5, 0.1 mL) in Pyrex tube, which was degassed by three freeze-pump-thaw cycles. The tube was then sealed and heated at 120 °C for 72 h. The resulting precipitate was collected, washed with THF and acetone, and dried at 120 °C under vacuum for 12 h to obtain PY-DHBD-COF.

2.3. Synthesis of Nb_2C QDs@PY-DHBD-COF

The Nb_2C QDs@PY-DHBD-COF heterostructures were synthesized by using a self-assembly method. In brief, the PY-DHBD-COF (20 mg) was dispersed in Nb_2C QDs aqueous solution (10 mL), and ultrasonication for 10 min to ensure homodisperse. Subsequently, the mixture was continuously stirred for 2 h, and centrifuged to obtain product and freeze-dried. According to the amount of Nb_2C QDs added (0.1, 0.2, 0.4, 0.6, 0.8 mg), the samples are denoted as NQPD-x (x = 1, 2, 3, 4, 5).

3. Results and discussion

The Nb_2C QDs were synthesized by employing as-prepared Nb_2C MXene as precursors via hydrothermal process (Fig. 1a and S1). The PY-DHBD-COF was served as pristine substrate for anchoring Nb_2C QDs, and synthesized from 1,4-dihydroxybenzidine with 1,3,6,8-tetra(4-formylphenyl)pyrene through Schiff-base condensation. The incorporation of Nb_2C QDs into PY-DHBD-COF was achieved through a straightforward self-assembly method, resulting in Nb_2C QDs@PY-DHBD-COF composites. The periodically dispersed anchoring sites for Nb_2C QDs are constructed by adjacent hydroxyl group and imine-N in the region of the PY-DHBD-COF structural unit [31]. With the increase of Nb_2C QDs loading amount, the samples are denoted as NQPD-x (x = 1, 2, 3, 4, 5).

The morphology and microstructure of Nb_2C QDs, PY-DHBD-COF and Nb_2C QDs@PY-DHBD-COF composite were characterized by transmission electron microscopy (TEM), and aberration-corrected high-angle annular dark-field scanning transmission electron microscopy (AC-HAADF-STEM). As described in Fig. 1b, the TEM image of Nb_2C QDs reveal the monodispersed morphology with an average size of 1.8 nm. Further, the atomic force microscopy (AFM) results manifest the average thickness of Nb_2C QDs is ~1.2 nm, which corresponds to around one layer of Nb_2C MXene (Fig. 1c) [32]. TEM images of the NQPD-3 (as a typical composite for further characterizations) demonstrate the successful anchoring of Nb_2C QDs on PY-DHBD-COF compared to the pure substrate (Fig. 1d and S2). In addition, scanning electron microscopy (SEM) images for PY-DHBD-COF and the NQPD-3 show similar hollow bar morphology (Fig. S3). The AC-STEM of NQPD-3 composite further indicates the lattice spacing of loaded Nb_2C QDs is 0.270 nm, corresponding to the (100) crystal plane (Fig. 1e) [33]. The AC-HAADF-STEM image further reveals the atomic structure arrangement of Nb_2C QDs in NQPD-3 composite (Fig. 1f). The bright dots within yellow circles accurately confirm the uniform dispersion of Nb_2C QDs on PY-DHBD-COF substrate (Fig. 1g). Furthermore, the energy-dispersive X-ray spectroscopy (EDX) elemental mappings indicate the homogeneous dispersion of atomic C, N, O, and Nb over the NQPD-3 (Fig. 1h). The above results demonstrate the successful assembly of Nb_2C QDs on PY-DHBD-COF.

The crystalline structure of PY-DHBD-COF and NQPD-x composites were characterized by powder X-ray diffraction (PXRD), in which distinct diffraction peaks at 3.2°, 4.6°, 6.4°, 9.6°, 12.5° and 23.4°, were corresponded to the (110), (020), (220), (330), (440) and (001) facets for PY-DHBD-COF, respectively [31]. The PXRD pattern of NQPD-x composites indicates that the introduction of Nb_2C QDs will not change the crystal structure of PY-DHBD-COF, which is attributed to the small size and low content of Nb_2C QDs (Fig. S4). Fourier transform infrared (FTIR) spectroscopy was further performed to investigate the chemical functional group structures of PY-DHBD-COF, and displayed characteristic vibration bands at 1628 cm^{-1} (C=N), confirming the formation of imine-linked PY-DHBD-COF (Fig. S5). Simultaneously, the NQPD-x nanohybrids exhibit distinct stretching bands originating from PY-DHBD-COF, further indicating the introduction of Nb_2C QDs will not alter the pristine structure of PY-DHBD-COF (Fig. S6).

To confirm the entrance of Nb_2C QDs into the pore channels and framework of PY-DHBD-COF, the Brunauer-Emmett-Teller (BET) surface area was evaluated by N_2 adsorption-desorption experiments at 77 K, revealing that the BET surface area of NQPD-3 composite was decreased when compared with PY-DHBD-COF (Fig. S7), which might be caused by the incorporation of Nb_2C QDs in PY-DHBD-COF pore channels (pore size of 2.7 nm) [34,35]. Furthermore, the thermogravimetric analysis shows the good thermal stability of PY-DHBD-COF and NQPD-3 hybrid upon heating to 350 °C (Fig. S8). The bonding structures and electronic states of PY-DHBD-COF and NQPD-3 were investigated by X-ray photoelectron spectroscopy (XPS) (Figs. S9–11). The C 1 s and N 1 s spectra of PY-DHBD-COF and NQPD-3 exhibit similar characteristic peaks, corresponding to the presence of units within the structure of PY-DHBD-COF. In contrast, the O 1 s spectrum exhibits a substantial difference after the introduction of Nb_2C QDs. The peak of C-OH in NQPD-3 hybrid exhibits a considerable shift to higher binding energy, and the peaks of new Nb-O groups appear, indicating that the introduction of Nb_2C QDs maintains close interaction with PY-DHBD-COF [36]. Furthermore, the high-resolution Nb 3d spectrum could be assigned to Nb-C and Nb-O species. The above XPS results show the strong interaction between C-OH and Nb_2C QDs sites in NQPD-3 heterostructure.

The photocatalytic activity of as-prepared catalysts was evaluated in pure water and real seawater under light illumination without sacrificial reagents (Fig. S12). As shown in Fig. 2a, the NQPD-x heterostructures exhibit significantly enhanced H_2O_2 yield than PY-DHBD-COF in pure water, indicating that the combination of Nb_2C QDs with PY-DHBD-COF contributes to the enhanced photocatalytic activity. By optimizing the

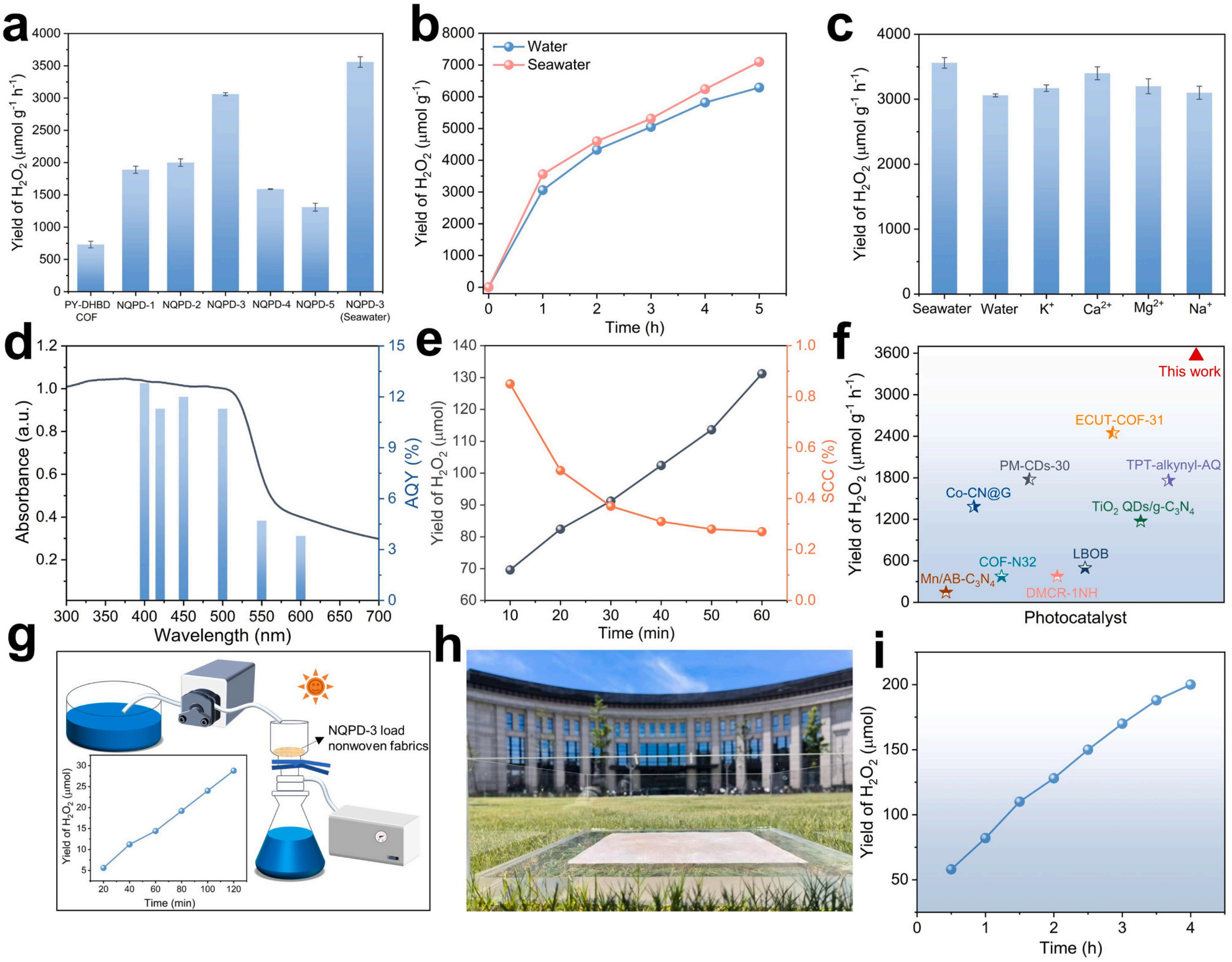

Fig. 2. (a) Photocatalytic performance of PY-DHBD-COF and NQPD-x in pure water and real seawater. (b) Time-dependent H_2O_2 photogeneration of NQPD-3. (c) H_2O_2 production rate in different salt solutions around the respective concentrations in seawater. (d) AQY of H_2O_2 photosynthesis over NQPD-3. (e) Changes in the amounts of H_2O_2 generated and SCC efficiency on NQPD-3. (f) Comparison of previously reported photocatalysts for H_2O_2 generation in seawater. (g) Dynamic H_2O_2 photoproduction in NQPD-3 loaded nonwoven fabric. (h) H_2O_2 photoproduction under natural sunlight in Fudan University Jiangwan campus using NQPD-3 loaded nonwoven fabric with the 0.3 m^2 reactor containing 1 L seawater. (i) Time-dependent H_2O_2 production in (h).

loading of Nb_2C QDs in heterostructures, the NQPD-3 exhibited the highest yield of H_2O_2 (3060 μmol g^{-1} h^{-1}) in pure water. Further, the photocatalytic activity of NQPD-3 catalyst was investigated in real seawater, manifesting a higher H_2O_2 amount was generated (3560 μmol g^{-1} h^{-1}) than that in pure water. The durability experiments reveal that NQPD-3 catalyst maintains continuous and stable production of H_2O_2 under photoirradiation for 5 h (Fig. 2b). The cycling experiments show that the catalytic performance of the NQPD-3 will be reduced to some extent, which is mainly caused by the pollution or carbon accumulation on the catalyst surface, affecting light absorption and carrier transport efficiency, thereby reducing catalytic performance (Fig. S13). In addition, the TEM, PXRD, FTIR, and XPS characterizations analysis showed that the morphology and chemical composition of NQPD-3 catalyst remained unchanged after long-term photocatalytic reaction and exhibited remarkable stability (Figs. S14–17).

To further compare the effects of main components in seawater on photocatalytic activity, the yield of H_2O_2 in separate ionic salts (KCl, $CaCl_2$, $MgCl_2$, and NaCl) were confirmed in Fig. 2c. It is observed that the presence of inorganic salts promotes H_2O_2 production in the range of seawater concentration, which can be attributed to the electron sink of oxygen-containing groups for the NQPD-3 heterostructure in presence of metal cations that boosts photocatalytic activity by attracting electrons [37,38]. In addition, the apparent quantum yield (AQY) of the NQPD-3 was evaluated under monochromatic light irradiation of 400, 420, 450, 500, 550 and 600 nm, respectively. As described in Fig. 2d, the AQY values are consistent with the variation trends of light response ability for the NQPD-3, and exhibits remarkable AQY of 12.8 % at 400 nm. Significantly, the solar-to-chemical conversion (SCC) efficiency of NQPD-3 heterostructure (0.27 %) under visible light irradiation is significantly higher than solar-to-biomass efficiency by plants (~0.1 %) (Fig. 2e) [39]. It is obvious that the photocatalytic H_2O_2 generation of NQPD-3 surpasses most of the previously reported photocatalysts in seawater (Fig. 2f) [14,15,37–43]. Furthermore, a photocatalytic device was elaborately fabricated by loading the NQPD-3 catalyst onto polypropylene nonwoven fabric, confirming the feasibility of practical application potential. The continuous flow photocatalytic production of H_2O_2 was evaluated using NQPD-3 loaded nonwoven fabric, exhibiting excellent photocatalytic H_2O_2 production (Fig. 2g). The scalable test for H_2O_2 photoproduction in outdoor environment was conducted under natural sunlight (Fig. 2h). The NQPD-3 loaded nonwoven fabric photocatalyst effectively produced H_2O_2 up to 200 μmol, demonstrating the practical value for large-scale H_2O_2 photoproduction (Fig. 2i).

Additionally, a typical dye photodegradation test by using RhB as a model on NQPD-3 loaded nonwoven fabric photocatalyst was conducted under natural sunlight irradiation, indicating the excellent photocatalytic dye degradation performance under practical conditions (Fig. S18).

Kelvin probe force microscopy (KPFM) was employed to explore the incorporation of Nb_2C QDs induced built-in electric field in NQPD-3 heterostructure (Fig. 3a and b). The surficial electrostatic potential of NQPD-3 (36 mV) is apparently higher than that of PY-DHBD-COF (17 mV), which contributes to a stronger built-in electric field accelerating charge transfer effectively [44–48]. In addition, the zeta potentials of PY-DHBD-COF and NQPD-3 are −7.4 and −18.0 mV, respectively, indicating the built-in electric field enhanced with the incorporation of Nb_2C QDs (Fig. 3c). The Nb_2C QDs in high-crystalline PY-DHBD-COF triggered a robust built-in electric field, which enabled continuous transportation of the photo-generated carriers to active sites. Furthermore, the photoluminescence (PL) and time-resolved photoluminescence (TRPL) spectra were conducted to further validate the efficient transfer and separation of photoinduced carriers. As depicted in Fig. 3d, the PL emission intensity of NQPD-3 hybrid is weaker than that of pristine PY-DHBD-COF, manifesting the incorporation of Nb_2C QDs in PY-DHBD-COF can greatly enhance the charge separation, and offer significant advantage in improving photocatalytic performance. The TRPL spectra reveal the lifetime of NQPD-3 composite (0.75 ns) is shorter than pristine PY-DHBD-COF (5.2 ns), indicating the incorporation of Nb_2C QDs with PY-DHBD-COF offers a new channel for photo-generated electrons transfer to Nb_2C QDs, and achieves efficient separation of photo-generated carriers.

Additionally, the transient photocurrent responses and electrochemical impedance spectra (EIS) further validate that enhanced built-in electric field promotes the migration of photo-generated carriers (Fig. 3e). The NQPD-3 exhibited the highest photocurrent density and lowest charge transfer resistance, verifying stronger built-in electric field suppressed the recombination of photo-generated carriers. The charge transfer pathway is confirmed by in-situ irradiation XPS, indicating the binding energy of N 1 s and O 1 s peak shifts positively by 0.2 eV, and the binding energy of Nb 3d peaks shift negatively by 0.3 eV under light illumination, compared to that in the dark (Fig. 3f-i). This

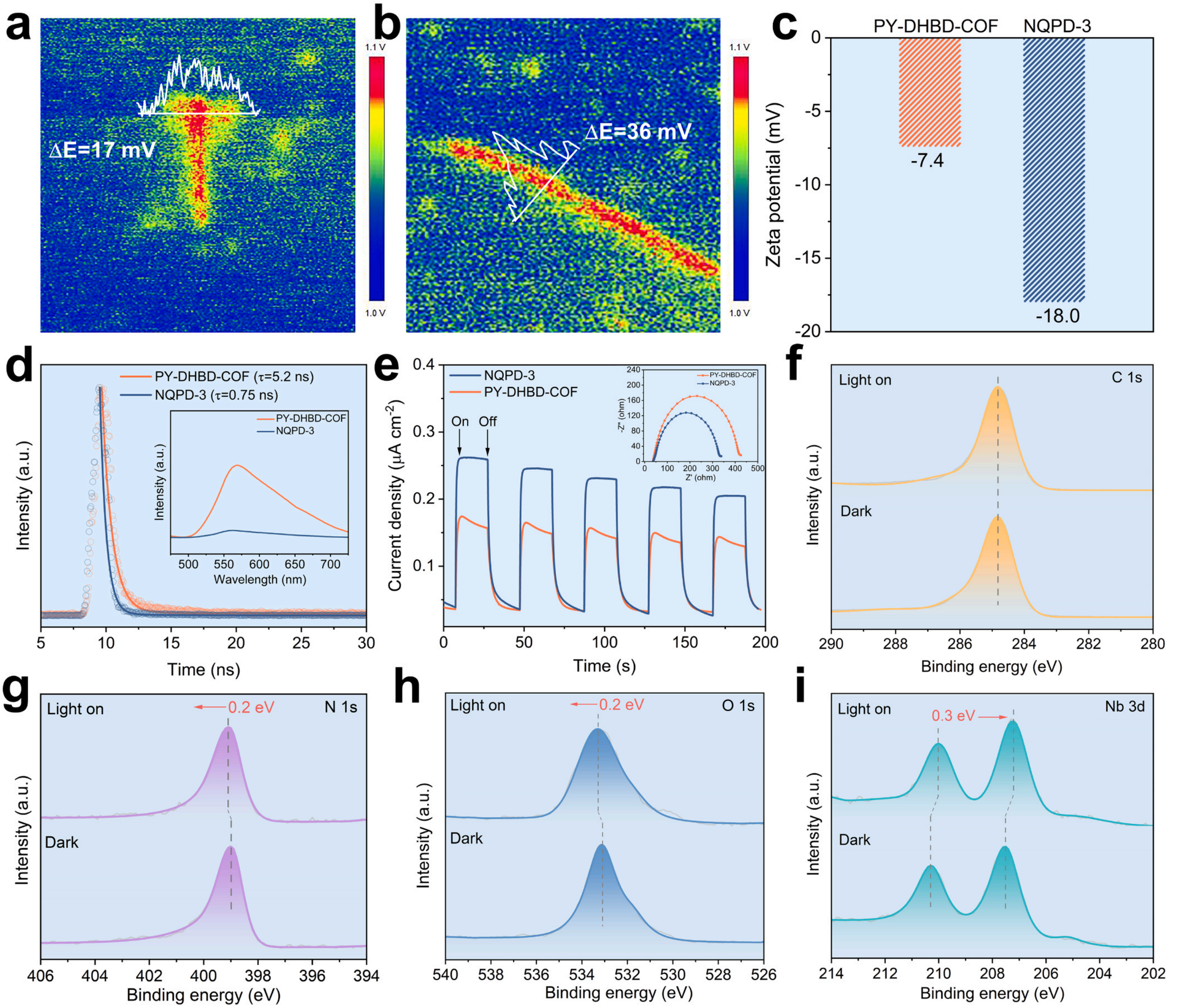

Fig. 3. (a, b) Surface potential of PY-DHBD-COF and NQPD-3 detected with KPFM. (c) Zeta-potentials of PY-DHBD-COF and NQPD-3. (d) PL and TRPL spectra of PY-DHBD-COF and NQPD-3. (e) EIS Nyquist plots and transient photocurrent response curves of PY-DHBD-COF and NQPD-3. (f-i) In-situ light illumination XPS spectra of NQPD-3.

finding verifies the surface charge transfer between the Nb_2C QDs and PY-DHBD-COF under in-situ light irradiation, and the photogenerated electron transfer from PY-DHBD-COF to Nb_2C QDs sites.

Femtosecond transient absorption spectroscopy (fs-TAS) was employed for investigating photoinduced charge transport within Nb_2C QDs@PY-DHBD-COF nanostructure. As depicted in Fig. 4a-d, the PY-DHBD-COF and NQPD-3 composite show negative signals at ~600 nm, corresponding to the ground state bleach (GSB). The weak absorption signal at ~750 nm belongs to the excited state absorption (ESA). The signal in NQPD-3 is particularly pronounced, which is attributed to the interaction between Nb_2C QDs and PY-DHBD-COF. Significantly, the lifetime of NQPD-3 composite is shorter than that of pure PY-DHBD-COF (Fig. 4e and f), indicating that the coupling of Nb_2C QDs with PY-DHBD-COF results in fewer photoelectrons available for diffusion and trapping processes, thereby shortening the corresponding lifetime [35].

The control experiments were conducted by employing different scavengers to trap active species in H_2O_2 photosynthesis process including benzoquinone (BQ, $\cdot O_2^-$), tert-butyl alcohol (TBA, ·OH), ethylene diamine tetra-acetic acid disodium salt (EDTA-2Na, h^+), $AgNO_3$ as the electron scavengers [49–52]. As described in Fig. 5a, the photocatalytic activity is severely hampered in the presence of BQ or $AgNO_3$, revealing the indispensable role of $\cdot O_2^-$ and e^-. Meanwhile, the introduction of TBA has negligible effect on H_2O_2 yield, manifesting that ·OH is not involved in the process of H_2O_2 generation. Based on these control experiments, the NQPD-3 follows the two-electron oxygen reduction reaction ($2e^-$ ORR) mechanism via $\cdot O_2^-$ intermediate for photocatalytic H_2O_2 generation. To further investigate the reaction mechanism of H_2O_2 photosynthesis over the NQPD-3, electron paramagnetic resonance (EPR) spectroscopy was conducted by using 5, 5-dimethyl-1-pyrroline N-oxide (DMPO) as the spin-trap agent (Fig. 5b). Under light irradiation, the signals of DMPO-$\cdot O_2^-$ are distinctly observed, confirming the $\cdot O_2^-$ is essential intermediate for H_2O_2 photosynthesis. Based on the above analysis, we conclude that the $\cdot O_2^-$ active species participate in the generation of H_2O_2 during photoreaction process.

To accurately identify the photocatalytic H_2O_2 generation process over NQPD-3 hybrid, the in-situ diffuse reflectance infrared Fourier transform spectroscopy (DRIFTS) was performed to detect real-time change in intermediates during $2e^-$ ORR process (Fig. 5c). The NQPD-3 displayed relatively obvious infrared absorption peaks at 818–850, 1150–1178, 1250–1290 and 1330–1388 cm^{-1}, which were attributed to adsorbed O_2, $\cdot O_2^-$, surface-adsorbed OOH* and HOOH* , respectively [53–55]. These in-situ experimental results indicate that $\cdot O_2^-$ is key intermediate in the process of H_2O_2 photoproduction. The optical and electronic properties for as-synthesized catalysts were comprehensively investigated. UV–visible diffuse reflectance spectroscopy (UV-Vis DRS) evaluated the optical capture capability and bandgap of PY-DHBD-COF and the NQPD-x, both of them possessed a broad absorption peak in the visible light region (Fig. S19). The UV-Vis DRS indicated the overall light absorption of the NQPD-x heterostructures was enhanced as the loading of Nb_2C QDs increased. Furthermore, the bandgap (E_g) values of PY-DHBD-COF and the NQPD-3 were 2.21 and 2.17 eV through the Tauc plots, which represented their semiconductor characteristics. In order to determine the energy band positions of catalysts, the Mott-Schottky (MS) electrochemical measurements were carried out, indicating that the conduction band (CB) potential of PY-DHBD-COF and NQPD-3 were located at −0.51 and −0.59 V vs NHE, respectively (Figs. S20 and 21). The schematic diagram of energy band structures is showed in Fig. 5d, exhibiting that both the CB and valence band (VB) position of the NQPD-3 shifted to negative potential after introducing Nb_2C QDs, and the CB position was lower than standard $2e^-$ ORR potential, ensuring sufficient reduction potential for H_2O_2 generation [56–58].

The $2e^-$ ORR process was further confirmed by rotating ring disk electrode (RRDE) experiment. The average electron transfer number (n) and H_2O_2 selectivity calculated within the potential range of 0.3–0.6 V vs RHE (Fig. 5e). The average electron transfer number of PY-DHBD-COF and the NQPD-3 are 2.90 and 2.34, respectively. The electron-transfer number of the NQPD-3 is closer to 2 than that of PY-DHBD-COF, indicating the superiority of the NQPD-3 in H_2O_2 photosynthesis

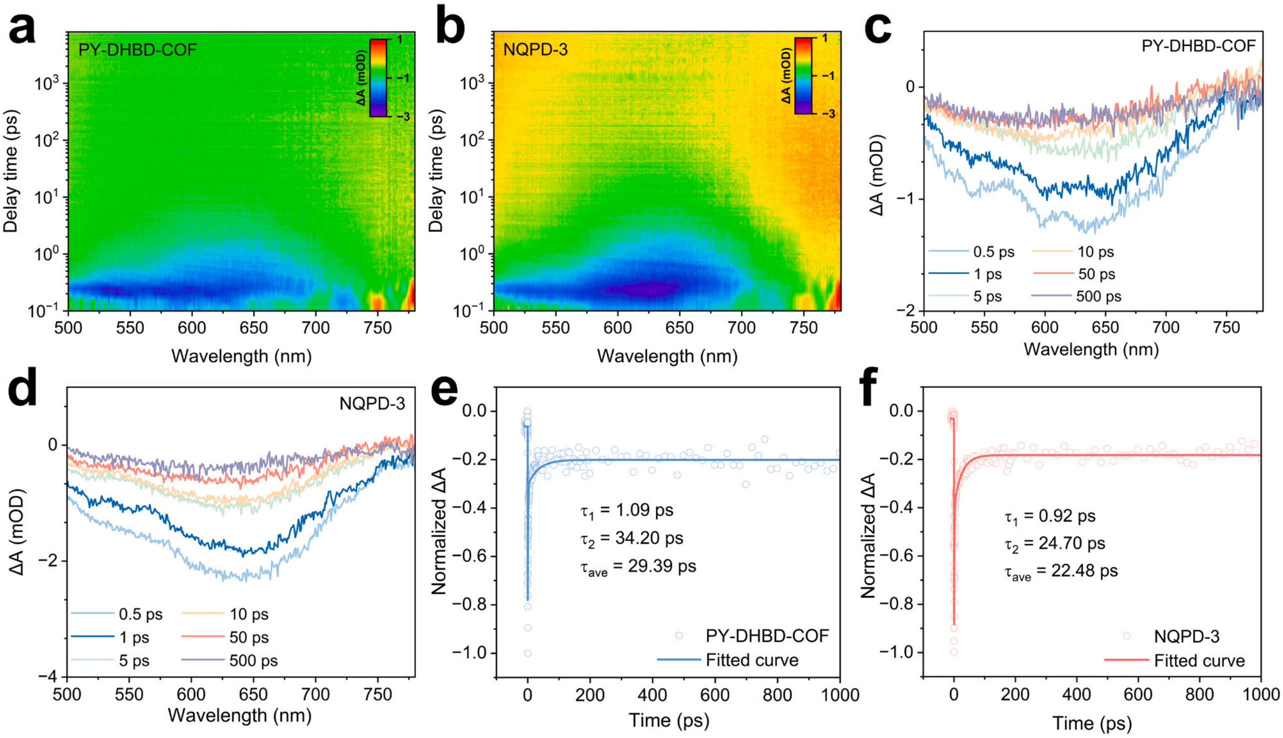

Fig. 4. (a, b) Three-dimensional contour plots of transient absorption spectra for PY-DHBD-COF and NQPD-3. (c, d) Transient absorption spectra recorded at indicated delay time. (e, f) Normalized decay kinetic curves for PY-DHBD-COF and NQPD-3.

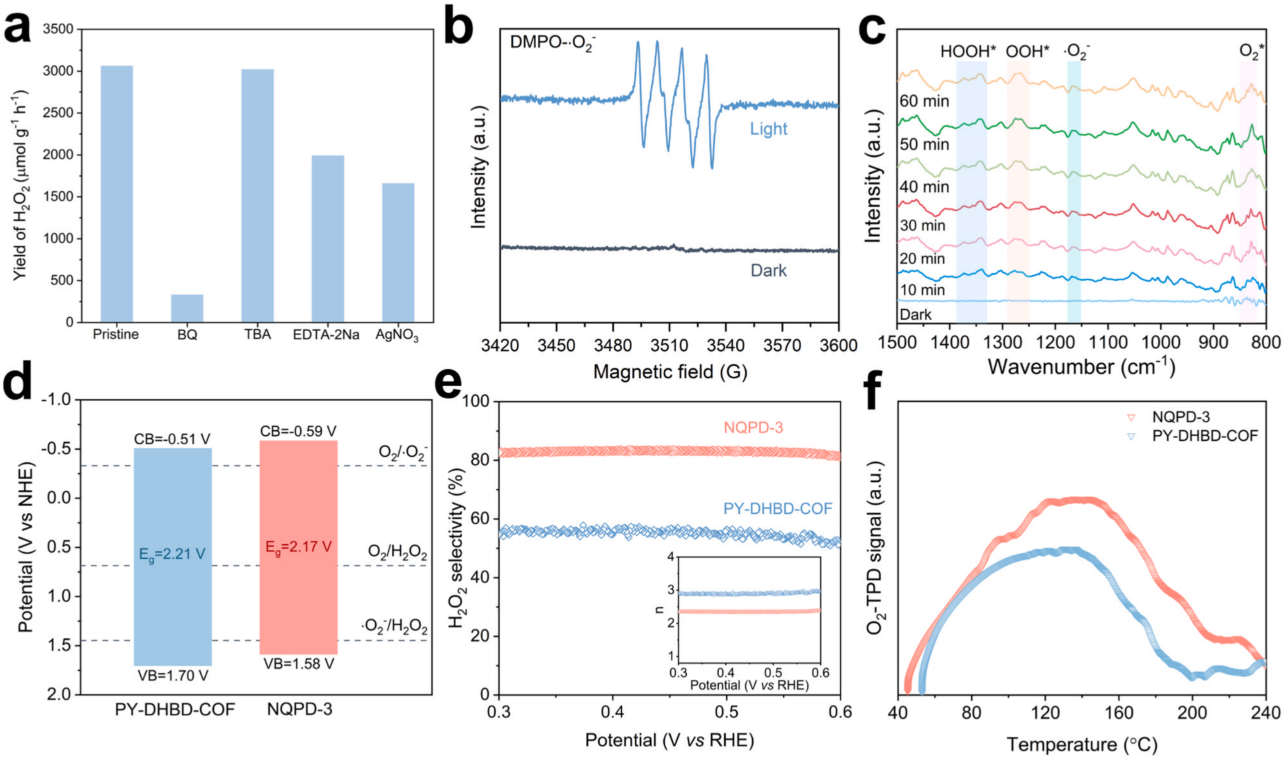

Fig. 5. (a) H_2O_2 production of NQPD-3 with different scavengers. (b) The EPR spectra of NQPD-3 with DMPO as electron-trapping agent. (c) In-situ DRIFTS spectra of NQPD-3 under light irradiation. (d) Band structure of PY-DHBD-COF and NQPD-3. (e) The H_2O_2 selectivity and electron-transfer number over PY-DHBD-COF and NQPD-3. (f) The O_2-TPD of PY-DHBD-COF and NQPD-3.

[59,60]. Additionally, the NQPD-3 exhibits a remarkable H_2O_2 selectivity of 82.9 %, suggesting the significant improvement compared to PY-DHBD-COF, further confirming that the 2e$^-$ ORR dominates on the NQPD-3 hybrid. Furthermore, the $^{18}O_2$ isotope experiment show that O_2 participates in the photocatalytic H_2O_2 formation of the NQPD-3 composite (Fig. S22). These results convincingly demonstrate the remarkable performance enhancement achieved by the integration of Nb_2C QDs into PY-DHBD-COF. Furthermore, the temperature-programmed desorption of O_2 (O_2-TPD) demonstrates the enhanced O_2 chemisorption ability for the NQPD-3 composite (Fig. 5f). The introduction of Nb_2C QDs significantly increases the number of active sites on the surface, and enhances the O_2 adsorption capacity. The O_2 desorption peak of the NQPD-3 shifts to higher temperature in relation to the pristine PY-DHBD-COF, indicating stronger interaction between O_2 and the NQPD-3 heterostructure.

To further achieve a more comprehensive understanding for the fundamental processes of photocatalytic H_2O_2 production on atomic scale, the density functional theory (DFT) calculations were conducted to analyze the O_2 adsorption, revealing that the adsorption energy of O_2 on NQPD-3 (-0.29 eV) is more negative compared to that of PY-DHBD-COF (0.32 eV), further confirming the higher stability of O_2 molecules adsorbed on the NQPD-3 composite (Fig. 6a) [61–63]. Therefore, the NQPD-3 exhibits pronounced advantage for the first step (O_2 adsorption) of the 2e$^-$ ORR process. The DFT calculation was also conducted to simulate the differential charge density distribution at the interface of NQPD-3 heterostructure (Fig. S23). The differential charge density distribution graph clearly manifests the aggregated electrons are focused on the Nb_2C QDs (blue region), while the deficient electrons are concentrated on the PY-DHBD-COF (yellow region). The planar-averaged charge density difference along with Z direction exhibits the change of charge density, indicating the electrons mainly transfer from PY-DHBD-COF to Nb_2C QDs. The DFT calculations further elucidated reaction process at the interface of NQPD-3 heterostructure. The optimized surface intermediates and corresponding free energy changes for each step of H_2O_2 production is shown in Fig. 6b. The reaction process of photocatalytic H_2O_2 production includes the following steps: 1) adsorption of O_2 molecules on the active sites of the NQPD-3 to form adsorbed *O_2; 2) transfer of electrons to the adsorbed *O_2 to reduce it to *OOH that is the rate-determining step in the 2e$^-$ ORR, and the free energy is calculated to be 0.29 eV; 3) combination of H$^+$ with *OOH to form *HOOH; and 4) hydrogenation of *HOOH to form H_2O_2 (Fig. 6c) [64–66]. Based on the abovementioned results, the introduction of Nb_2C QDs sites can achieve the high O_2 adsorption and conducive to the reduction of O_2.

4. Conclusion

In summary, we have successfully synthesized Nb_2C QDs sites immobilized on pyrene-based covalent organic framework (Nb_2C QDs@PY-DHBD-COF, NQPD-x) heterostructures for efficient non-sacrificial H_2O_2 photosynthesis from air and natural seawater. Impressively, the optimal NQPD-3 catalyst achieved a record H_2O_2 yield of 3560 μmol g^{-1} h^{-1}, and AQY of 12.8 % at 400 nm together with SCC efficiency of 0.27 %, superior to currently reported photocatalysts for H_2O_2 photosynthesis from natural seawater. The combination of experimental characterizations and DFT calculations collectively confirm that the excellent photocatalytic performance is attributed to the robust built-in electric field modulated by Nb_2C QDs, and the synergistic effect of the heterostructures, which promotes photogenerated carriers transfer and optimizes O_2 adsorption. This work broadens the scope for designing advanced photocatalysts for sustainable H_2O_2 production from air and natural seawater.

CRediT authorship contribution statement

Yamei Huang: Conceptualization, Methodology, Investigation, Validation, Writing - original draft. **Xinglin Wang:** Writing - review & editing. **Huihui Zhang:** Validation, formal analysis. **Linlin Gao:**

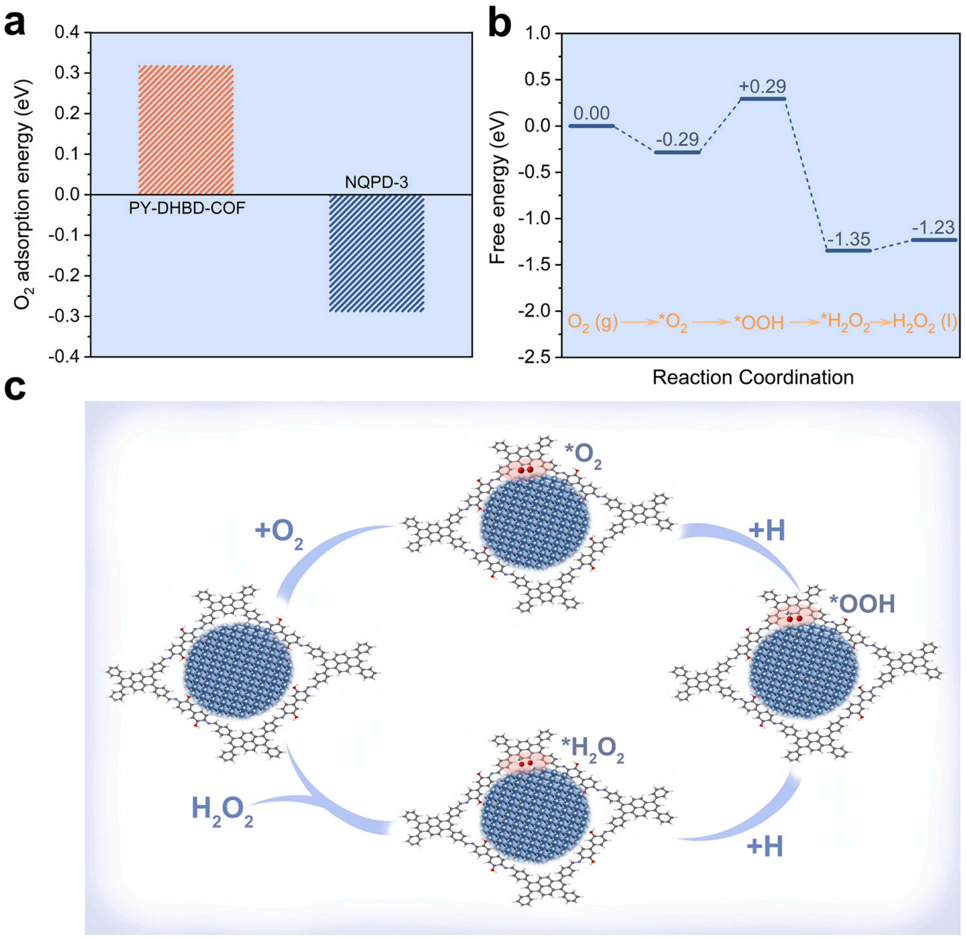

Fig. 6. (a) Optimum O_2 adsorption energies of PY-DHBD-COF and NQPD-3. (b) The free energy diagram for H_2O_2 photosynthesis on NQPD-3. (c) Schematic illustration of photocatalytic H_2O_2 production over NQPD-3.

Validation. **Jiayi Meng:** Formal analysis. **Yifan Liao:** Validation. **Quanmei Zhou:** Formal analysis. **Yuchen Wei:** Validation. **Baoning Zong:** Project administration, Writing - review & editing. **Hexing Li:** Supervision, Writing - review & editing. **Wei-Lin Dai:** Funding acquisition, Project administration, Supervision, Writing - review & editing, Visualization.

Declaration of Competing Interest

The authors declare no competing financial interest.

Acknowledgement

This work was supported by the National Key Research and Development Program of China (2021YFA1501404), Natural Science Foundation of Shanghai (22ZR1404200), and the Science and Technology Commission of Shanghai Municipality (2024ZDSYS02).

Appendix A. Supporting information

Supplementary data associated with this article can be found in the online version at doi:10.1016/j.apcatb.2025.125262.

Data availability

Data will be made available on request.

References

[1] C. Xia, Y. Xia, P. Zhu, L. Fan, H. Wang, Direct electrosynthesis of pure aqueous H_2O_2 solutions up to 20% by weight using a solid electrolyte, Science 366 (2019) 226–231.

[2] Y. Zhao, P. Zhang, Z. Yang, L. Li, J. Gao, S. Chen, T. Xie, C. Diao, S. Xi, B. Xiao, C. Hu, W. Choi, Mechanistic analysis of multiple processes controlling solar-driven H_2O_2 synthesis using engineered polymeric carbon nitride, Nat. Commun. 12 (2021) 3701.

[3] S. Qu, H. Wu, Y.H. Ng, Clean production of hydrogen peroxide: a heterogeneous solar-driven redox process, Adv. Energy Mater. 13 (2023) 2301047.

[4] H. Ou, Y. Jin, B. Chong, J. Bao, S. Kou, H. Li, Y. Li, X. Yan, B. Lin, G. Yang, Hydroxyl-bonded Co single atom site on boroncarbonitride surface realizes nonsacrificial H_2O_2 synthesis in the near-infrared region, Adv. Mater. 36 (2024) 2404851.

[5] S. Yan, Y. Li, X. Yang, X. Jia, J. Xu, H. Song, Photocatalytic H_2O_2 generation reaction with a benchmark rate at air-liquid-solid joint interfaces, Adv. Mater. 36 (2024) 2307967.

[6] J.M. Campos-Martin, G. Blanco-Brieva, J.L. Fierro, Hydrogen peroxide synthesis: an outlook beyond the anthraquinone process, Angew. Chem. Int. Ed. 45 (2006) 6962–6984.

[7] X. Zhang, S. Cheng, C. Chen, X. Wen, J. Miao, B. Zhou, M. Long, L. Zhang, Keto-anthraquinone covalent organic framework for H_2O_2 photosynthesis with oxygen and alkaline water, Nat. Commun. 15 (2024) 2649.

[8] Y. Deng, W. Liu, R. Xu, R. Gao, N. Huang, Y. Zheng, Y. Huang, H. Li, X.Y. Kong, L. Ye, Reduction of superoxide radical intermediate by polydopamine for efficient hydrogen peroxide photosynthesis, Angew. Chem. Int. Ed. 63 (2024) e202319216.

[9] H. Hou, X. Zeng, X. Zhang, Production of hydrogen peroxide by photocatalytic processes, Angew. Chem. Int. Ed. 59 (2020) 17356–17376.

[10] Y. Sun, L. Han, P. Strasser, A comparative perspective of electrochemical and photochemical approaches for catalytic H_2O_2 production, Chem. Soc. Rev. 49 (2020) 6605–6631.

[11] D. Tan, R. Zhuang, R. Chen, M. Ban, W. Feng, F. Xu, X. Chen, Q. Wang, Covalent organic frameworks enable sustainable solar to hydrogen peroxide, Adv. Funct. Mater. 34 (2023) 2311655.

[12] T. Yang, D. Zhang, A. Kong, Y. Zou, L. Yuan, C. Liu, S. Luo, G. Wei, C. Yu, Robust covalent organic framework photocatalysts for H_2O_2 production: linkage position matters, Angew. Chem. Int. Ed. 63 (2024) e202404077.

[13] K. Mase, M. Yoneda, Y. Yamada, S. Fukuzumi, Seawater usable for production and consumption of hydrogen peroxide as a solar fuel, Nat. Commun. 7 (2016) 11470.

[14] P. Ren, T. Zhang, N. Jain, H.Y.V. Ching, A. Jaworski, G. Barcaro, S. Monti, J. Silvestre-Albero, V. Celorrio, L. Chouhan, A. Rokicinska, E. Debroye, P. Kustrowski, S. Van Doorslaer, S. Van Aert, S. Bals, S. Das, An atomically dispersed Mn-photocatalyst for generating hydrogen peroxide from seawater via the water oxidation reaction (WOR), J. Am. Chem. Soc. 145 (2023) 16584–16596.

[15] A. Gopakumar, P. Ren, J. Chen, B.V. Manzolli Rodrigues, H.Y. Vincent Ching, A. Jaworski, S.V. Doorslaer, A. Rokicinska, P. Kustrowski, G. Barcaro, S. Monti, A. Slabon, S. Das, Lignin-supported heterogeneous photocatalyst for the direct generation of H_2O_2 from seawater, J. Am. Chem. Soc. 144 (2022) 2603–2613.

[16] C. Wu, Z. Teng, C. Yang, F. Chen, H.B. Yang, L. Wang, H. Xu, B. Liu, G. Zheng, Q. Han, Polarization engineering of covalent triazine frameworks for highly efficient photosynthesis of hydrogen peroxide from molecular oxygen and water, Adv. Mater. 34 (2022) 2110266.

[17] Z. Yong, T. Ma, Solar-to-H_2O_2 catalyzed by covalent organic frameworks, Angew. Chem. Int. Ed. 62 (2023) e202308980.

[18] P. Dong, X. Xu, T. Wu, R. Luo, W. Kong, Z. Xu, S. Yuan, J. Zhou, J. Lei, Stepwise protonation of three-dimensional covalent organic frameworks for enhancing hydrogen peroxide photosynthesis, Angew. Chem. Int. Ed. 63 (2024) e202405313.

[19] D. Chen, W. Chen, Y. Wu, L. Wang, X. Wu, H. Xu, L. Chen, Covalent organic frameworks containing dual O_2 reduction centers for overall photosynthetic hydrogen peroxide production, Angew. Chem. Int. Ed. 62 (2023) e202217479.

[20] R. Liu, Y. Chen, H. Yu, M. Položij, Y. Guo, T.C. Sum, T. Heine, D. Jiang, Linkage-engineered donor-acceptor covalent organic frameworks for optimal photosynthesis of hydrogen peroxide from water and air, Nat. Catal. 7 (2024) 195–206.

[21] Y. Mou, X. Wu, C. Qin, J. Chen, Y. Zhao, L. Jiang, C. Zhang, X. Yuan, E. Huixiang Ang, H. Wang, Linkage microenvironment of azoles-related covalent organic frameworks precisely regulates photocatalytic generation of hydrogen peroxide, Angew. Chem. Int. Ed. 62 (2023) e202309480.

[22] J. Sun, H. Sekhar Jena, C. Krishnaraj, K. Singh Rawat, S. Abednatanzi, J. Chakraborty, A. Laemont, W. Liu, H. Chen, Y.Y. Liu, K. Leus, H. Vrielinck, V. Van Speybroeck, P. Van Der Voort, Pyrene-based covalent organic frameworks for photocatalytic hydrogen peroxide production, Angew. Chem. Int. Ed. 62 (2023) e202216719.

[23] L. Stegbauer, S. Zech, G. Savasci, T. Banerjee, F. Podjaski, K. Schwinghammer, C. Ochsenfeld, B.V. Lotsch, Tailor-made photoconductive pyrene-based covalent organic frameworks for visible-light driven hydrogen generation, Adv. Energy Mater. 8 (2018) 1703278.

[24] Y. Hou, P. Zhou, F. Liu, Y. Lu, H. Tan, Z. Li, M. Tong, J. Ni, Efficient photosynthesis of hydrogen peroxide by cyano-containing covalent organic frameworks from water, air and sunlight, Angew. Chem. Int. Ed. 63 (2024) e202318562.

[25] C. Shu, X. Yang, L. Liu, X. Hu, R. Sun, X. Yang, A.I. Cooper, B. Tan, X. Wang, Mixed-linker strategy for the construction of sulfone-containing D-A-A covalent organic frameworks for efficient photocatalytic hydrogen peroxide production, Angew. Chem. Int. Ed. 63 (2024) e202403926.

[26] W. Zeng, X. Ye, Y. Dong, Y. Zhang, C. Sun, T. Zhang, X. Guan, L. Guo, MXene for photocatalysis and photothermal conversion: synthesis, physicochemical properties, and applications, Coord. Chem. Rev. 508 (2024) 215753.

[27] X. Xie, N. Zhang, Positioning MXenes in the photocatalysis landscape: competitiveness, challenges, and future perspectives, Adv. Funct. Mater. 30 (2020) 2002528.

[28] G. Murali, J.K. Reddy Modigunta, Y.H. Park, J.H. Lee, J. Rawal, S.Y. Lee, I. In, S. J. Park, A review on MXene synthesis, stability, and photocatalytic applications, ACS Nano 16 (2022) 13370–13429.

[29] H. Deng, Y. Hui, C. Zhang, Q. Zhou, Q. Li, H. Du, D. Hao, G. Yang, Q. Wang, MXene-derived quantum dots based photocatalysts: synthesis, application, prospects, and challenges, Chin. Chem. Lett. 35 (2024) 109078.

[30] K. Zhang, D. Li, H. Cao, Q. Zhu, C. Trapalis, P. Zhu, X. Gao, C. Wang, Insights into different dimensional MXenes for photocatalysis, Chem. Eng. J. 424 (2021) 130340.

[31] Y. Li, L. Yang, H. He, L. Sun, H. Wang, X. Fang, Y. Zhao, D. Zheng, Y. Qi, Z. Li, W. Deng, In situ photodeposition of platinum clusters on a covalent organic framework for photocatalytic hydrogen production, Nat. Commun. 13 (2022) 1355.

[32] D. Huang, Y. Xie, D. Lu, Z. Wang, J. Wang, H. Yu, H. Zhang, Demonstration of a white laser with V_2C MXene-based quantum dots, Adv. Mater. 31 (2019) 1901117.

[33] L. Yang, J. Du, J. Deng, N.H.M. Sulaiman, X. Feng, C. Liu, X. Zhou, Defective Nb_2C MXene cocatalyst on TiO_2 microsphere for enhanced photocatalytic CO_2 conversion to methane, Small 20 (2024) 2307007.

[34] Y. Yang, Q. Guo, Q. Li, L. Guo, H. Chu, L. Liao, X. Wang, Z. Li, W. Zhou, Carbon quantum dots confined into covalent triazine frameworks for efficient overall photocatalytic H_2O_2 production, Adv. Funct. Mater. 34 (2024) 2400612.

[35] Y. He, P. Hu, J. Zhang, G. Liang, J. Yu, F. Xu, Boosting artificial photosynthesis: CO_2 chemisorption and S-scheme charge separation via anchoring inorganic QDs on COFs, ACS Catal. 14 (2024) 1951–1961.

[36] C. Zhu, Y. Yao, Q. Fang, S. Song, B. Chen, Y. Shen, Unveiling the dynamic evolution of single-atom Co sites in covalent triazine frameworks for enhanced H_2O_2 photosynthesis, ACS Catal. 14 (2024) 2847–2858.

[37] Q. Wu, J. Cao, X. Wang, Y. Liu, Y. Zhao, H. Wang, Y. Liu, H. Huang, F. Liao, M. Shao, Z. Kang, A metal-free photocatalyst for highly efficient hydrogen peroxide photoproduction in real seawater, Nat. Commun. 12 (2021) 483.

[38] W. Wang, Q. Song, Q. Luo, L. Li, X. Huo, S. Chen, J. Li, Y. Li, S. Shi, Y. Yuan, X. Du, K. Zhang, N. Wang, Photothermal-enabled single-atom catalysts for high-efficiency hydrogen peroxide photosynthesis from natural seawater, Nat. Commun. 14 (2023) 2493.

[39] F. Liu, P. Zhou, Y. Hou, H. Tan, Y. Liang, J. Liang, Q. Zhang, S. Guo, M. Tong, J. Ni, Covalent organic frameworks for direct photosynthesis of hydrogen peroxide from water, air and sunlight, Nat. Commun. 14 (2023) 4344.

[40] P. Das, G. Chakraborty, J. Roeser, S. Vogl, J. Rabeah, A. Thomas, Integrating bifunctionality and chemical stability in covalent organic frameworks via one-pot multicomponent reactions for solar-driven H_2O_2 production, J. Am. Chem. Soc. 145 (2023) 2975–2984.

[41] Y. Liao, L. Guo, L.L. Gong, Q.Y. Zhang, D. Zhao, Y. Jia, R. Hua, F. Luo, Regulating benzene ring number as connector in covalent organic framework for boosting photosynthesis of H_2O_2 from seawater, Nano Lett. 24 (2024) 3819–3825.

[42] H. Zhang, S. Wang, J. Tian, X. Bai, Photocatalytic hydrogen peroxide production from seawater over graphitic carbon nitride supported titanium dioxide quantum dots, J. Environ. Chem. Eng. 12 (2024) 112290.

[43] H. Yan, M. Shen, Y. Shen, X.D. Wang, W. Lin, J. Pan, J. He, Y.X. Ye, X. Yang, F. Zhu, J. Xu, J. He, G. Ouyang, Spontaneous exciton dissociation in organic photocatalyst under ambient conditions for highly efficient synthesis of hydrogen peroxide, PNAS 119 (2022) e2202913119.

[44] L. Jian, Y. Dong, H. Zhao, C. Pan, G. Wang, Y. Zhu, Highly crystalline carbon nitrogen polymer with a strong built-in electric fields for ultra-high photocatalytic H_2O_2 production, Appl. Catal. B Environ. Energy 342 (2024) 123340.

[45] L. Li, X. Lv, Y. Xue, H. Shao, G. Zheng, Q. Han, Custom-design of strong electron/proton extractor on COFs for efficient photocatalytic H_2O_2 production, Angew. Chem. Int. Ed. 63 (2024) e202320218.

[46] J. Xu, W. Li, W. Liu, J. Jing, K. Zhang, L. Liu, J. Yang, E. Zhu, J. Li, Y. Zhu, Efficient photocatalytic hydrogen and oxygen evolution by side-group engineered benzodiimidazole oligomers with strong built-in electric fields and short-range crystallinity, Angew. Chem. Int. Ed. 61 (2022) e202212243.

[47] J. Cheng, W. Wang, J. Zhang, S. Wan, B. Cheng, J. Yu, S. Cao, Molecularly tunable heterostructured co-polymers containing electron-deficient and -rich moieties for visible-light and sacrificial-agent-free H_2O_2 photosynthesis, Angew. Chem. Int. Ed. 63 (2024) e202406310.

[48] Y. Xu, W. Hou, K. Huang, H. Guo, Z. Wang, C. Lian, J. Zhang, D. Wu, Z. Lei, Z. Liu, L. Wang, Engineering built-in electric field microenvironment of CQDs/g-C_3N_4 heterojunction for efficient photocatalytic CO_2 reduction, Adv. Sci. 11 (2024) 2403607.

[49] H. Yu, F. Zhang, Q. Chen, P.K. Zhou, W. Xing, S. Wang, G. Zhang, Y. Jiang, X. Chen, Vinyl-group-anchored covalent organic framework for promoting the photocatalytic generation of hydrogen peroxide, Angew. Chem. Int. Ed. 63 (2024) e202402297.

[50] Z. Li, X. Shi, H. Cheng, Y. Song, Y. Jiao, S. Shi, J. Gao, J. Hou, Atomically dispersed iron active sites on covalent organic frameworks for artificial photosynthesis of hydrogen peroxide, Adv. Energy Mater. 14 (2024) 2302797.

[51] X. Li, G. Zhang, N. Li, Q. Xu, H. Li, J. Lu, D. Chen, Self-floating photocatalytic system for highly efficient hydrogen peroxide production and organic synthesis on carbon dots decorated conjugated microporous polymer, Adv. Funct. Mater. 34 (2024) 2316773.

[52] L. Cao, C. Wang, H. Wang, X. Xu, X. Tao, H. Tan, G. Zhu, Rationally designed cyclooctatetrathiophene-based porous aromatic frameworks (COTh-PAFs) for efficient photocatalytic hydrogen peroxide production, Angew. Chem. Int. Ed. 63 (2024) e202402095.

[53] C. Yang, S. Wan, B. Zhu, J. Yu, S. Cao, Calcination-regulated microstructures of donor-acceptor polymers towards enhanced and stable photocatalytic H_2O_2 production in pure water, Angew. Chem. Int. Ed. 61 (2022) e202208438.

[54] Y.Y. Tang, X. Luo, R.Q. Xia, J. Luo, S.K. Peng, Z.N. Liu, Q. Gao, M. Xie, R.J. Wei, G. H. Ning, D. Li, Molecular engineering of metal-organic frameworks for boosting photocatalytic hydrogen peroxide production, Angew. Chem. Int. Ed. 63 (2024) e202408186.

[55] Y. Luo, B. Zhang, C. Liu, D. Xia, X. Ou, Y. Cai, Y. Zhou, J. Jiang, B. Han, Sulfone-modified covalent organic frameworks enabling efficient photocatalytic hydrogen peroxide generation via one-step two-electron O_2 reduction, Angew. Chem. Int. Ed. 62 (2023) e202305355.

[56] Y. Zhao, Y. Kondo, Y. Kuwahara, K. Mori, H. Yamashita, Two-phase reaction system for efficient photocatalytic production of hydrogen peroxide, Appl. Catal. B Environ. Energy 351 (2024) 123945.

[57] T. He, Y. Zhao, Covalent organic frameworks for efficient hydrogen peroxide production, EnergyChem 6 (2024) 100121.

[58] E. Zhou, F. Wang, X. Zhang, Y. Hui, Y. Wang, Cyanide-based covalent organic frameworks for enhanced overall photocatalytic hydrogen peroxide production, Angew. Chem. Int. Ed. 63 (2024) e202400999.

[59] P. Li, F. Ge, Y. Yang, T. Wang, X. Zhang, K. Zhang, J. Shen, 1D covalent organic frameworks triggering highly efficient photosynthesis of H_2O_2 via controllable modular design, Angew. Chem. Int. Ed. 63 (2024) e202319885.

[60] C.W. Bai, L.L. Liu, J.J. Chen, F. Chen, Z.Q. Zhang, Y.J. Sun, X.J. Chen, Q. Yang, H. Q. Yu, Circumventing bottlenecks in H_2O_2 photosynthesis over carbon nitride with iodine redox chemistry and electric field effects, Nat. Commun. 15 (2024) 4718.

[61] H. Peng, H. Yang, J. Han, X. Liu, D. Su, T. Yang, S. Liu, C.W. Pao, Z. Hu, Q. Zhang, Y. Xu, H. Geng, X. Huang, Defective $ZnIn_2S_4$ nanosheets for visible-light and sacrificial-agent-free H_2O_2 photosynthesis via O_2/H_2O Redox, J. Am. Chem. Soc. 145 (2023) 27757–27766.

[62] X. Zhang, H. Su, P. Cui, Y. Cao, Z. Teng, Q. Zhang, Y. Wang, Y. Feng, R. Feng, J. Hou, X. Zhou, P. Ma, H. Hu, K. Wang, C. Wang, L. Gan, Y. Zhao, Q. Liu, T. Zhang,

K. Zheng, Developing Ni single-atom sites in carbon nitride for efficient photocatalytic H_2O_2 production, Nat. Commun. 14 (2023) 7115.

[63] W. Wu, Z. Li, S. Liu, D. Zhang, B. Cai, Y. Liang, M. Wu, Y. Liao, X. Zhao, Pyridine-based covalent organic frameworks with pyridyl-imine structures for boosting photocatalytic H_2O_2 production via one-step $2e^-$ oxygen reduction, Angew. Chem. Int. Ed. 63 (2024) e202404563.

[64] C. Feng, J. Luo, C. Chen, S. Zuo, Y. Ren, Z.-P. Wu, M. Hu, S. Ould-Chikh, J. Ruiz-Martínez, Y. Han, H. Zhang, Cooperative tungsten centers in polymeric carbon nitride for efficient overall photosynthesis of hydrogen peroxide, Energy Environ. Sci. 17 (2024) 1520–1530.

[65] J.-P. Liao, M. Zhang, P. Huang, L.-Z. Dong, T.-T. Ma, G.-Z. Huang, Y.-F. Liu, M. Lu, S.-L. Li, Y.-Q. Lan, Flexible units induced three-dimensional covalent organic frameworks with a heteromotif molecular junction for photocatalytic H_2O_2 production, ACS Catal. 14 (2024) 3778–3787.

[66] Z. Teng, Q. Zhang, H. Yang, K. Kato, W. Yang, Y.-R. Lu, S. Liu, C. Wang, A. Yamakata, C. Su, B. Liu, T. Ohno, Atomically dispersed antimony on carbon nitride for the artificial photosynthesis of hydrogen peroxide, Nat. Catal. 4 (2021) 374–384.